The University of Southern Mississippi
The Aquila Digital Community

Faculty Publications

4-15-2001

Seasonal Variation of the North Atlantic Current

Max I. Yaremchuk
University of Hawaii

Dmitri A. Nechaev
University of Southern Mississippi, dmitri.nechaev@usm.edu

Keith R. Thompson
Dalhousie University

Follow this and additional works at: http://aquila.usm.edu/fac_pubs

Part of the Marine Biology Commons

Seasonal variation of the North Atlantic Current

Max I. Yaremchuk

International Pacific Research Center, University of Hawaii, Honolulu, Hawaii

Dmitri A. Nechaev

Department of Marine Science, University of Southern Mississippi, Stennis Space Center, Mississippi

Keith R. Thompson

Department of Oceanography, Dalhousie University, Halifax, Nova Scotia, Canada

Abstract. The seasonal circulation of the upper 1000 m of the North Atlantic between 40°–55°N and 20°–40°W is calculated using the traditional dynamic method and a circulation model with a density field that evolves with the flow. The model is of finite difference form and is based on dynamics that describe the nonlinear evolution of the ocean at low Rossby number. The model is controlled by initial and boundary conditions that include air-sea buoyancy and momentum fluxes. The model is run in two ways: with controls specified directly from observations and with controls inferred by the assimilation of all available data. These data include surface drifter trajectories, sea levels from the TOPEX/Poseidon altimeter, Bunker air-sea fluxes, and the Levitus climatological monthly means of temperature and salinity. We conclude that the North Atlantic Current transport is 40 ± 18 Sv with seasonal variations of the order of 2 Sv. The mean vertical transport out of the region is 2 ± 9 Sv and is subject to seasonal variations of 2 Sv. Overall, these estimates are in good agreement with integral North Atlantic Current features derived from independent long-term measurements made in the region over the past decade. The optimal ocean state has a volume transport across the western boundary of 51 ± 3 Sv with a maximum transport of 61 ± 5 Sv in April–May and a minimum of 42 ± 3 Sv in October–November. This western inflow is compensated by mean outflows of 28 ± 2 (east), 16 ± 2 (north), 5 ± 2 (south), and 1.8 ± 0.4 Sv out of the domain at 1000 m. Sensitivity studies show that nonlinear mixing and seasonality are important in determining the overall circulation. Specifically, steady boundary forcing leads to annual mean transports that are 15–25% smaller than transports obtained with seasonal forcing. Winter convection is also shown to play a significant role in determining the overall circulation pattern.

1. Introduction

This study is focused on the seasonal variability of the transports and fluxes associated with circulation and hydrography in the upper 1000 m of the central North Atlantic between 40°–55°N and 40°–20°W (Figure 1). There is general agreement on a mean northeastward flow of relatively warm water through the region. However, there is not agreement on the magnitude of the heat and volume transports or the details of the circulation [e.g., *Sy et al.*, 1992; *Schmitz and McCartney*, 1993; *Rossby*, 1996]. For example, recent estimates of the transport of the North Atlantic Current (NAC) across the western boundary of our study area range from 25 to 40 Sv [e.g., *Baryshevskaya*, 1985; *Krauss*, 1986; *Krauss et al.*, 1990; *Sy et al.*, 1992; *Rossby*, 1996]. Most of these estimates were obtained by applying the traditional dynamical method to hydrographic data collected during synoptic surveys. They are therefore subject to errors associated with the choice of the velocity reference level and aliasing of the region's vigorous eddy activity.

One way to improve traditional estimates of the ocean's

state and its fluxes is to assimilate the available data into an ocean circulation model. A number of such studies have now been carried out for the North Atlantic [e.g., *Provost and Salmon*, 1986; *Martel and Wunsch*, 1993; *Marotzke and Wunsch*, 1993; *Nechaev et al.*, 1995]. This approach has now generally replaced purely statistical schemes such as optimal interpolation. The main reason is that statistical schemes require information on the correlation scales of the variables to be mapped. Even if one accepts the concept of correlation scales as meaningful in an ocean that is statistically nonstationary and nonhomogeneous, there are usually insufficient data to estimate the correlation functions accurately. This leaves the statistical schemes strongly dependent on dubious assumptions about characteristic length scales and timescales.

Assimilation methods for estimating the ocean state are usually based on a prior probability distribution, $\mathcal{P}$ say, of the differences between observations and the true model predictions. It is usually more straightforward to specify the covariance structure of these differences than the covariance structure of the ocean state, as required by optimal interpolation. The dynamics can be considered as a nonlinear operator $\mathcal{A}$ that maps a vector of control variables $\mathbf{C}$ onto the model state vector $\mathbf{X} = \mathcal{A}(\mathbf{C})$. In the present study the control vector $\mathbf{C}$
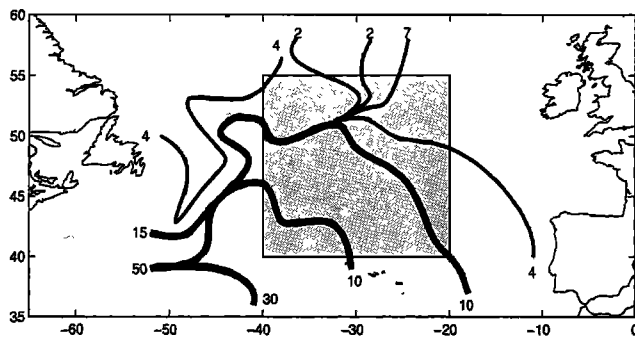
Figure 1. Transport in the top 1000 m of the northern North Atlantic by the Labrador Current, Gulf Stream, and North Atlantic Current according to *Dietrich et al.* [1975]. Numbers denote transports in Sverdrups (10^6 m^3 s^{-1}). The shaded rectangle defines the model domain.

includes the initial and boundary conditions of the ocean circulation model. Starting from a first guess C_f, it is usually possible to find an optimal control vector C_o that maximizes $\mathcal{P}$. The dynamics then provide an optimal estimate of the complete ocean state through the mapping $X_o = \mathcal{A}(C_o)$. Results of this type of analysis include not only interpolated fields that satisfy the assumed dynamical constraints (either exactly to some prescribed level of accuracy) but also confidence regions for functions of the state vector that could include, for example, heat transports and vertical velocities.

In the present study we use data assimilation to estimate the seasonal variation of the hydrography, velocity, and boundary fluxes of the central North Atlantic. The assimilated data include monthly means of air-sea fluxes, gridded temperatures and salinities, sea surface heights measured by the TOPEX/Poseidon altimeter, and surface drifter tracks. The dynamics have been simplified by assuming the space scales are longer than one internal Rossby radius and the timescales are longer than 1 month. The dynamical constraints remain nonlinear, however. One important consequence of this nonlinearity is that the assimilation scheme is sensitive to C_f and the parameters required to fix $\mathcal{P}$.

We first estimate the seasonal changes in the circulation from the hydrography. Specifically, the flow in the top 1000 m is estimated from temperature and salinity data by (1) assuming a level of no motion at 1000 m and (2) taking the surface as the reference level and specifying it with sea levels measured by the TOPEX/Poseidon altimeter. We show that the assumption of no motion at 1000 m is a poor assumption in this region. We also show for both assumptions 1 and 2 the density field is incompatible with the diagnosed flow fields.

The ocean state is then estimated using a nonlinear circulation model that allows the density field to evolve with the flow. The initial and boundary conditions are specified directly from the observed temperatures, salinities, and air-sea fluxes. Although the resulting flow fields are consistent with the assumed dynamics, the estimated fields exhibit uncontrollable error growth.

Finally, we combine, in an optimal way, the dynamical constraints of the circulation model and the available climatological data. The assimilation algorithm is similar to the data inversion schemes of *Schlitzer* [1993], *Martel and Wunsch* [1993], and *Mercier et al.* [1993], which have been used successfully to reconstruct the steady state large-scale circulation of

the Atlantic. The major difference in our formulation is its ability to accommodate seasonal changes. The governing equations are applied as strong constraints. They include geostrophic balance below a surface layer controlled by Ekman dynamics, conservation of volume, hydrostatic balance, and buoyancy conservation with vertical convective adjustment. One of the relatively novel features of the present analysis is the calculation of the full Hessian matrix, which allows us to construct confidence intervals for the estimated ocean state.

The observations are described briefly in section 2, and the various schemes for estimating the ocean state are described in section 3. We discuss our estimates of the state and check them against published transport values and independent current measurements in section 4. The sensitivity of the solutions to the temporal resolution of the boundary forcing and the mixing parameterizations is discussed in section 5. Conclusions are given in section 6.

2. Observations

The observations include temperature and salinity at standard depths, sea level from the TOPEX/Poseidon altimeter, air-sea fluxes, and surface drifter trajectories. All data types have been averaged into monthly means. To quantify the overall variability of the monthly means, including their seasonal cycles, we have calculated their standard deviation σ_{obs} by averaging through time and across the model domain. To estimate model error at a fixed location, we used a Fourier expansion to describe the temporal variability of the monthly means as follows:

$$\phi(t) = \sum_{k=1}^{L} a_k q_k(t), \tag{1}$$

where ϕ stands for an observed monthly mean for month t. The first Fourier component q_1 is constant through time and its amplitude a_1 is the mean. The next pair of components, q_2 and q_3, define the annual cycle. Higher-order terms define harmonics of the annual cycle. The standard deviation of ϕ after removal of the seasonal variability using (1) is denoted by σ_{mod}. It generally decreases with increasing L. To quantify the uncertainty in the individual monthly means, we have also estimated their standard error σ_d by taking into account the intramonthly variability and observational errors.

2.1. Temperature and Salinity

Monthly means were extracted from the climatology compiled by *Levitus et al.* [1994a] and *Levitus and Boyer* [1994] (made available through Web site http://www.nodc.noaa.gov). Despite the well-known problems with that data set we selected it primarily because of the large amount of data underlying this climatology. On the average it has $n = 22.7$ hydrocasts per month per square degree in the region of interest. Alternative data sets, such as the North Atlantic climatology of *Losier et al.* [1995], although derived through isopycnal interpolation and not so heavily smoothed, are characterized by $n \sim 3$–4. In the balance between the formal error bars and subjective degree of realism we chose the former, assuming that isobaric averaging and extra smoothing will not strongly affect the seasonal cycle of the net fluxes and transports associated with NAC variability.

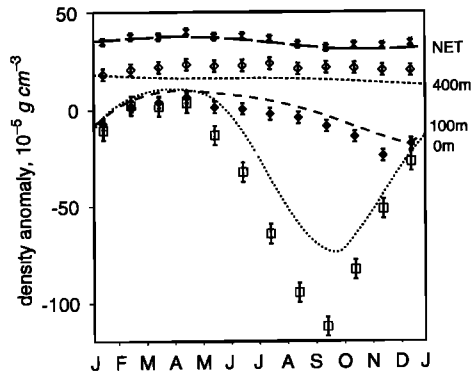Temperature and salinity of the *Levitus et al.* [1994a, 1994b]

Figure 2. Monthly means of observed density at various depths as a function of month. The short vertical lines through the symbols show the standard errors. The continuous lines are densities predicted by experiment A0.

and *Levitus and Boyer* [1994] data set were converted into density using the standard United Nations Educational, Scientific, and Cultural Organization formula [*Fofonoff and Millard*, 1983]. The seasonal cycle of density is well defined at the surface, but it attenuates with depth to the point that it is almost nonexistent at 400 m (Figure 2, diamonds). Stratification in the top 100 m is close to neutral from January to April, presumably the result of winter convection and enhanced wind

mixing at this time of year. The minimum density over the top 100 m occurs progressively later in the year with increasing depth: at 30 m the minimum is in September, and at 100 m it is in November. Horizontal maps of density at 100 m are dominated by an overall north-south gradient, with the lowest densities generally occurring in fall (Figure 3). The maximum vertical shears implied by these maps of density and the thermal wind relationship are of order 10 m s^{-1} in 1000 m.

The standard deviation of the monthly means drops by a factor of 10 from the sea surface to 1000 m (Table 1, row labeled σ_{obs}). Most of the variation in density is due to the seasonal cycle. The standard deviations of the density after removal of the annual cycle (i.e., (1) with $L = 3$) are typically reduced by a factor of 4, but the depth dependence remains (Table 1, row labeled σ_{mod}).

The standard errors of the monthly densities (σ_d) were estimated from the standard errors of temperature and salinity under the assumption that the fluctuations of temperature and salinity are statistically independent and sufficiently small to neglect nonlinearities in the equation of state. The σ_d are 5–10 times smaller than the standard deviation of the monthly densities at the same depth (Table 1, compare the rows labeled σ_d and σ_{obs}).

2.2. Air-Sea Fluxes

Wind stresses were extracted from the climatological atlas of *Isemer and Hasse* [1987] (made available through Web site
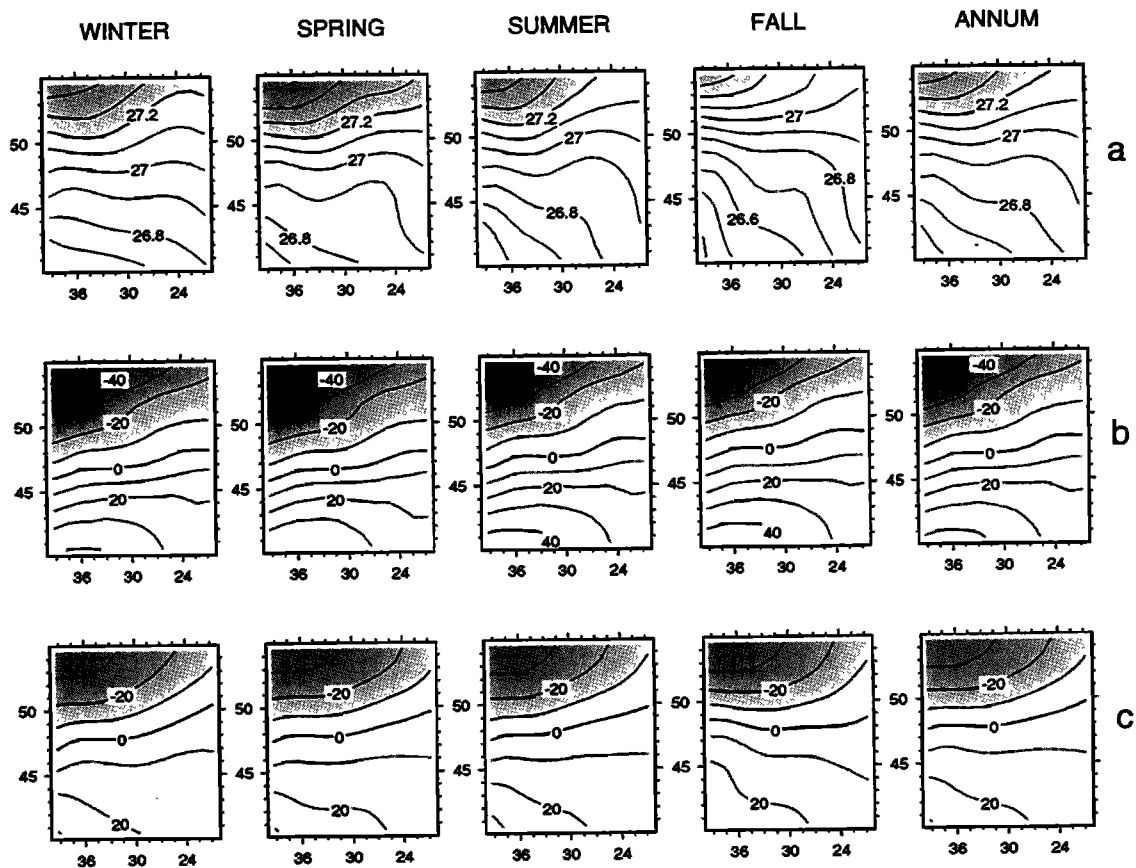

Figure 3. Seasonal means of the observations: (a) *Levitus et al.* [1994a, 1994b] and *Levitus and Boyer* [1994] density data at 100 m in kg m^{-3}, (b) sea level from the TOPEX/Poseidon altimeter in centimeters, and (c) dynamic height derived from the *Levitus et al.* [1994a, 1994b] and *Levitus and Boyer* [1994] climatology under the assumption of no motion at 1000 m in centimeters.

Table 1. Standard Deviations of the Monthly Means of Observations and Related Quantities[a]

| | Density, ρ | | | | | | | |
	30 m	100 m	400 m	1000 m	B	ζ	τ	$\Delta\rho$
σ_{obs}	49.	23.	22.	4.6	48.	25.	0.44	⋯
σ_{mod}	10.	5.0	2.6	1.4	6.1	0.7	0.33	⋯
σ_d	4.2	3.0	3.0	0.7	14.	20.	0.20	2.2
σ_{md}	8.7	5.5	2.5	1.4	14.	7.1	0.35	1.2
σ_p	1.0	1.3	0.8	0.6	4.	5.	0.15	1.0

[a]The abbreviations are as follows: σ_{obs}, standard deviation of all monthly means at the sea surface or the level specified; σ_{mod}, standard deviation after removing annual cycle; σ_d, standard error of the monthly means; σ_{md}, standard deviation of the difference between A1 predictions and observations; σ_p, standard deviation of the state estimated by experiment A1; ρ, water density in 10^{-5} g cm^{-3}; B, surface buoyancy flux in 10^{-8} g cm^{-2} s^{-1}; ζ, sea level in cm; τ, wind stress in cm^2 s^{-2}; and $\Delta\rho$, change in water density over one year integration in 10^{-5} g cm^{-3}.

http://www.scd.ucar.edu (Figure 4)). The standard deviation of the monthly stresses is 0.44 cm^2 s^{-2} (Table 1, σ_{obs}). Wind stress is more variable about the annual cycle than, for example, the surface density ($\sigma_{obs}/\sigma_{mod} \approx 1$, Table 1). Uncertainties in wind stress arise from errors in the wind observations and uncertainties in the nonlinear drag law used to convert wind into stress. Our estimate of the standard error of the monthly means is 0.2 cm^2 s^{-2} (Table 1, σ_d).

Buoyancy flux at the sea surface was not directly available from *Isemer and Hasse* [1987]. We calculated it from the monthly means of net surface heat flux $H(\mathbf{x}, t)$ using

$$B = \alpha c_p^{-1} \rho_0 H, \tag{2}$$

where α is the thermal expansion coefficient, c_p is the heat capacity of seawater, and ρ_0 is a reference surface density. This calculation assumes that the influence of the freshwater flux is negligible in this region [e.g., *Schmitt et al.*, 1989]. Our computed buoyancy fluxes (Figure 4) differ from the fields of
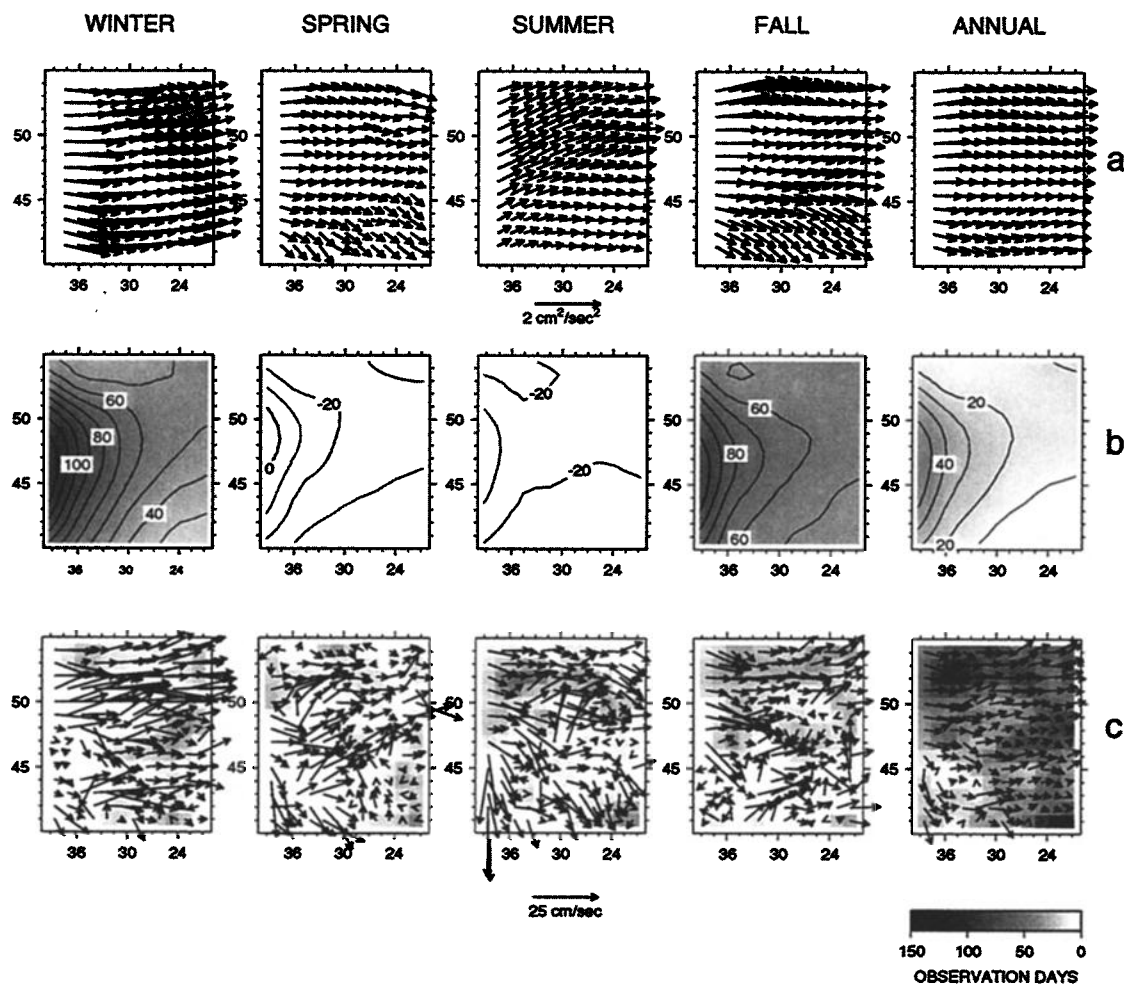

Figure 4. Seasonal means of the observations: (a) wind stress (scale shown), (b) surface buoyancy flux in 10^{-8} g cm^2 s^{-1}, and (c) surface drifter velocities (scale shown).

Schmitt et al. [1989] by only a few percent, an amount that is well within the error bars of the estimated heat flux. The buoyancy fluxes are dominated by the seasonal cycle ($\sigma_{obs}/\sigma_{mod} \approx 8$, Table 1).

According to the inverse calculation of *Isemer et al.* [1989] we set the buoyancy flux error level σ_d of 14×10^{-8} g cm^{-2} s^{-1}. This value may be interpreted as the combined effect of a heat flux uncertainties of 35 W m^{-2} and a freshwater flux uncertainties of 30 cm yr^{-1}. As noted by *Marotzke and Wunsch* [1993], the errors in the buoyancy flux estimates could be even larger.

2.3. Sea Level

Sea level measured by the TOPEX/Poseidon altimeter was obtained from the University of Texas at Austin Center for Space Research (through the Web site ftp://ftp.csr.utexas.edu). The TOPEX/Poseidon database includes a 4 year mean dynamic topography (September 1992 to December 1996) and 10 day sea level anomaly fields about this mean. We computed monthly mean sea level fields by averaging the 10 day fields for a given month and then adding the mean field.

The surface topography is dominated by a fairly steady north-south gradient of 1 m across the model domain (Figure 3). This drop implies surface geostrophic currents of the order of 5 cm s^{-1}. Sea level changes at a fixed location are dominated by the annual cycle, ($\sigma_{obs}/\sigma_{mod} \approx 35$, Table 1). The annual cycle can be explained in large part by changes in dynamic height relative to 1000 m. If we take 2×10^{-4} g cm^{-3} as a measure of the seasonal changes in density over the top 1000 m (Table 1), the standard deviation of the associated dynamic height is 20 cm, close to that observed by the TOPEX/Poseidon altimeter ($\sigma_{obs} = 25$ cm, Table 1).

We have treated separately the standard errors of the mean surface topography and the variability about this mean. The major uncertainty in the mean topography is the JGM-3 geoid model, which introduces errors ranging from 17 and 22 cm. Standard errors of the annual cycle and higher harmonics are estimated to be 4 cm on the basis of information gathered from the available documentation. (More information on the processing of the TOPEX/Poseidon data is given by *Tapley et al.* [1994].)

2.4. Drifter Trajectories

The trajectories of 2167 surface drifters that moved through the model domain between January 1991 and March 1995 were obtained from the Marine Environmental Data Service (Canada). Most of the drifters were drogued between 5 and 15 m and therefore sample the velocity in the surface Ekman layer. The total number of position fixes was 82,852, the number of drifter years was 25.3, and the average time spent by drifters in a typical model grid cell was 47 days. Differences in consecutive positions were used to estimate velocity. Outliers were defined by speeds exceeding 150 cm s^{-1}, and they were discarded prior to the calculation of monthly mean velocities for each model grid cell.

Four years of drifter data are insufficient to map accurately the seasonal mean surface velocity (Figure 4, note the number of empty cells). The annual mean pattern is more spatially coherent and suggests an overall eastward transport in the surface layer of about 10 cm s^{-1}.

To estimate standard error of the monthly mean drifter velocities for each cell, we assumed (1) individual velocities were statistically independent and (2) their standard errors

scaled with the time between the pair of fixes used to calculate the velocity. The standard error for a given cell and month was found to vary with the number of drifter days, τ, according to 10 cm s$^{-1} \times \sqrt{\tau_0/\tau}$ with $\tau_0 \sim 180$ days.

3. Methods for Estimating Ocean State

The traditional dynamic method and our circulation model are now described in terms of a modification of the set of equations proposed by *Welander* [1959]:

$$f(\mathbf{k} \times \mathbf{u}) = -\frac{1}{\rho_0}\nabla p + \nu\partial_{zz}\mathbf{u}, \tag{3}$$

$$\partial_z p + g\rho = 0, \tag{4}$$

$$\nabla \cdot \mathbf{u} + \partial_z w = 0, \tag{5}$$

$$\partial_t \rho + \nabla \cdot (\mathbf{u}\rho) + \partial_z(w\rho) = A_l\Delta\rho + \partial_z(A_\nu\partial_z\rho) + \hat{\Pi}(\rho), \tag{6}$$

where f is the Coriolis parameter, $(\mathbf{u}, w) \equiv (u, v, w)$ is the velocity vector, ν is the vertical eddy viscosity, p is pressure, g is acceleration due to gravity, A_l and A_ν are lateral and vertical eddy diffusion coefficients, and Δ is the horizontal Laplacian operator. Unstable density profiles are suppressed by the convective adjustment operator $\hat{\Pi}(\rho)$ (see Appendix A). To integrate this system, we must specify the initial condition

$$\rho(\mathbf{x}, z, 0) = \rho^0 \tag{7}$$

and boundary conditions

$$\nu\partial_z\mathbf{u}(\mathbf{x}, 0, t) = \tau, \tag{8}$$

$$A_\nu\partial_z\rho(\mathbf{x}, 0, t) = B, \tag{9}$$

$$p(\mathbf{x}, 0, t) = \rho_0 g\zeta, \tag{10}$$

$$w(\mathbf{x}, 0, t) = 0, \tag{11}$$

$$\rho(\partial V, z, t) = \rho_\ell, \tag{12}$$

$$\rho(\mathbf{x}, -h, t) = \rho_b, \tag{13}$$

$$\partial_z\mathbf{u}(\mathbf{x}, -h, t) = 0. \tag{14}$$

The initial density is denoted by ρ^0, wind stress is denoted by τ, buoyancy flux is denoted by B, and sea level is denoted by ζ. Densities on the lateral boundaries (∂V) and bottom boundary ($z = -h$) are denoted by ρ_ℓ and ρ_b, respectively.

Welander's [1959] equations have been used with considerable success in studies of large-scale circulation [e.g., *Needler*, 1967; *Stommel and Schott*, 1977; *Wunsch*, 1994]. The system of equations (3)–(14) is slightly more general than the system proposed by *Welander* [1959] in that we have allowed for (1) temporal changes, (2) horizontal diffusion in the density equation, and (3) nonadiabatic processes in the upper mixed layer. Scale analysis shows that the modified system applies to space scales and timescales longer than 200 km and 30 days, respectively. These scales are consistent with spatial and temporal resolution of the data, and in fact, they impose physical limitation on the horizontal resolution of the grid (section 3.2) precluding recovery of the more detailed flow pattern shown in Figure 1.

3.1. Dynamic Method

This method is based on (3)–(5) and boundary conditions (8), (10), (11), and (14). This reduced set of equations is a

linear mapping of τ, ζ, and ρ into the three-dimensional velocity field $(\mathbf{u}, w)$. In the absence of direct measurements of sea surface elevation it is often assumed that isobaric surfaces are level at some depth $z = -h$. Integration of the hydrostatic equation from $z = -h$ to 0 then gives p at all depths and ζ in particular. If the sea surface topography is known, it can be used to specify p at the sea surface and the integration of the hydrostatic equation gives p and $(\mathbf{u}, w)$ at all depths as before. Neither approach takes into account buoyancy flux or the density conservation constraint (6).

3.2. Prognostic Model Without Data Assimilation

We will show that the velocity field calculated using the dynamical method is inconsistent with the observed density field. To overcome this limitation, we developed a numerical circulation model based on a discretized form of the modified Welander equations. The integration scheme is a semi-implicit, conservative finite difference scheme defined on a standard Arakawa C grid (see Figure 1 for model domain). The model grid is specified in a Cartesian coordinate system defined under the β plane approximation. Spatial derivatives are approximated by central differences, and leapfrog time stepping is used for temporal derivatives. The scheme is implicit with respect to vertical advection and diffusion of density. All other processes are treated explicitly. The horizontal grid spacing is uniform in x and y and equal to 111 km. The vertical levels are identical to the ρ levels used in the *Levitus et al.* [1994a, 1994b] and *Levitus and Boyer* [1994] climatology: 10, 30, 50, 75, 100, 150, 200, 250, 300, 400, 500, 700, and 1000 m. The model time step is typically 4 days, and the integration is carried out for 1 year.

The paucity of density and surface flux data does not allow variations on timescales <1 month to be resolved. The prognostic model, on the other hand, requires boundary conditions to be updated every time step. To overcome this mismatch in temporal resolution, the time variation of the model's boundary variables is approximated by a truncated Fourier expansion of the form (1): if $L = 1$, the boundary forcing is constant though time; if $L = 3$, it varies with an annual cycle about this mean.

The run of the prognostic circulation model without assimilation of data will henceforth be referred to as experiment A0. Parameter settings for this, and other runs, are given in Table 2. Note, vertical diffusivity varies with z according to $A_v = A_{v0}$ $\exp(z/h_0) + A_{vh}$, where $h_0 = 30$ m and $A_{vh} = 0.1$ cm^2 s^{-1}.

3.3. Prognostic Model With Data Assimilation

The assimilation problem is to find a solution to the modified *Welander* [1959] equations that minimizes the following cost function:

$$J = J_{obs} + J_{reg},$$

where J_{obs} is proportional to the weighted mean square difference between observations and predictions and J_{reg} is made up of regularization terms.

J_{obs} is made up of the following seven components.

1. $\sum_{m=1}^{12} \int_V W_\rho(z)(\rho_m^* - \bar{\rho}^m)^2 \, dv$: The observed density for month m and the corresponding model prediction are denoted by ρ_m^* and $\bar{\rho}^m$, respectively. The summation is over all months of the year, and the integral is over the whole model

Table 2. List of Numerical Experiments[a]

Experiment	L	A_l	A_{v0}	Sea Level	Convection
A0	3	20	2	TP$_2$	CA
A1	3	20	2	TP$_1$	CA
B1	1	20	2	TP$_1$	CA
B2	5	20	2	TP$_1$	CA
B3	7	20	2	TP$_1$	CA
C1	3	2	2	TP$_1$	CA
C2	3	8	2	TP$_1$	CA
C3	3	40	2	TP$_1$	CA
C4	3	20	4	TP$_1$	CA
E1	3	20	2	TP$_2$	...
E2	3	20	2	TP$_2$	CD

[a]The abbreviations are as follows: L, number of terms in the Fourier representation of the boundary forcing; A_l, horizontal viscosity in 10^6 cm^2 s^{-1}; A_{v0}, vertical viscosity at surface in cm^2 s^{-1}; TP$_1$, TOPEX/ Poseidon monthly anomalies and long-term mean treated separately; TP$_2$, TOPEX/Poseidon monthly anomalies and long-term mean combined into a single measurement; CA, conventional hydrostatic adjustment procedure; and CD, mixing simulated by nonlinear diffusion.

domain. $W_\rho(x)$ is a depth-dependent weight factor, and the overbar denotes time average over the month m.

2. $\sum_{m=1}^{12} \int_S W_B(B_m^* - \bar{B}^m)^2 \, dS$, which is similar to component 1 but for surface buoyancy B. The weight factor W_B is invariant with respect to time of year and location.

3. $\sum_{m=1}^{12} \int_S W_u(\mathbf{x}, m)|\mathbf{u}_m^* - \bar{\mathbf{u}}^m|^2 \, dS$, which is similar to component 2 but for surface currents. The observed surface flow, inferred from the bin-averaged drifter velocities, is denoted by $\mathbf{u}_m^*$; the current velocity in the top (0–10 m) layer is denoted by $\bar{\mathbf{u}}^m$. The weight factor W_u varies with grid cell and time of year, depending on the quality and number of drifter observations in each bin average.

4. $\sum_{m=1}^{12} \int_S W_\tau(\tau_m^* - \bar{\tau}^m)^2 \, dS$, which is similar to component 2 but for wind stress τ. The weight factor W_τ is constant.

5. $\sum_{m=1}^{12} \int_S W_\zeta(\zeta_d^* - \bar{\zeta}^m)^2 \, dS$, which is similar to component 2 but for sea level. Dynamic height calculated from the hydrographic data under the assumption of no flow at 1000 m is denoted by ζ_d^*; the monthly mean sea level from the model is denoted by $\bar{\zeta}^m$. The weight factor W_ζ is constant.

6. $\sum_{m=1}^{12} \int_S W_{\zeta'}[(\zeta_m^* - \bar{\zeta}^*) - \overline{(\zeta - \bar{\zeta})^m}]^2 \, dS$, which is similar to component 2 but for sea level anomalies about the long-term mean (denoted by overbar). Monthly sea level anomalies measured by the TOPEX/Poseidon altimeter are denoted by $\zeta_m^* - \bar{\zeta}^*$; the corresponding monthly anomalies from the model are denoted by $\overline{(\zeta - \bar{\zeta})^m}$. The weight factor $W_{\zeta'}$ is constant.

7. $\sum_{m=1}^{12} \int_S W_{\bar{\zeta}}(\bar{\zeta}^* - \bar{\zeta})^2 \, dS$, which is similar to component 2 but for long-term mean sea level. Mean sea surface topography measured by the TOPEX/Poseidon altimeter is denoted by $\bar{\zeta}^*$; the corresponding mean topography from the model is denoted by $\bar{\zeta}$. The weight factor $W_{\bar{\zeta}}$ is constant.

We have assumed that the W matrices above are diagonal. The reciprocals of its diagonal elements can be interpreted as variances of the difference between observations and the true model prediction. In general, we assumed that these variances are due to observation and model error and approximated them by $\sigma_d^2 + \sigma_{mod}^2$. Note that for some variables we have sufficient information to allow W to vary with location and time (e.g., W_ρ and W_u). For dynamic height we used a weighting $W_\zeta^{-1/2}$ of 15 cm in accord with the assumed error levels in the *Levitus et al.* [1994a, 1994b] and *Levitus and Boyer* [1994]

data and uncertainty in the magnitude of large-scale currents at 1000 m (which we assumed to be 5 cm s^{-1}).

The second group in the cost function J_{reg} is made up of the following six regularization terms.

1. Term 1, $\int_V P_\rho(z)(\rho^T - \rho^0)^2 \, dv$, penalizes differences between the initial density field ρ^0 and the density at the end of 1 year's integration, ρ^T. It enforces periodicity as a weak constraint. The strength of the regularization term changes with depth.

2. Term 2, $\int_S \Sigma_{k=1}^L R_B(k)(\Delta a_k)^2 \, ds$, penalizes small-scale features in the horizontal distribution of the surface buoyancy flux. Here Δ denotes the Laplacian operator, and a_k is the kth Fourier amplitude of the surface buoyancy flux at a given location. The strength of this regularization term changes with Fourier component k.

3. Term 3, $\int_S \Sigma_{k=1}^L R_\tau(k)(\Delta a_k)^2 \, ds$, is the same as term 2 but for wind stress.

4. Term 4, $\int_S \Sigma_{k=1}^L R_\zeta(k)(\Delta a_k)^2 \, ds$, is the same as term 2 but for sea level.

5. Term 5, $\int_V \Sigma_{m=1}^{12} R_\rho(z)(\Delta \bar{\rho}^m)^2 \, dv$, is similar to term 2 but for density. The weight factor R_ρ is a function of depth.

6. Term 6, $\int_S \Sigma_{m=1}^{12} R_u(\Delta \bar{U}^m)^2 \, ds$, is the same as term 2 but for the monthly depth mean flow $\bar{U}^m$. The weight factor R_u is constant.

Setting the regularization weighting is difficult and depended, in part, on previous model runs to assess the likely size of squared Laplacians. To specify P_ρ, we estimated the variability of the density field at timescales longer than a year from the long-term trends of surface temperature and salinity in the study area region [Levitus et al., 1994b; A. Clarke, personal communication, 1996]. Typical changes in temperature and salinity over the last several decades have been about 0.05°C and 0.003 psu per year, respectively. This leads us to take $P_\rho^{-1/2} = 2 \times 10^{-5} \text{ g cm}^{-3} \text{ yr}^{-1}$.

The discretized form of the governing equations (3)–(6) and their boundary conditions (7)–(14) are applied as strong constraints on the large-scale fields of ρ, p, $\mathbf{u}$, and w. The state vector $\mathbf{X}$ is made up of the gridded values of these four fields at all model time steps. The number of grid positions for ρ, p, $\mathbf{u}$, and w is 11,430. The model takes 84 time steps during a 1 year integration, and so, the length of $\mathbf{X}$ is 11,430 × 84 = 960,120. To integrate the model, it is necessary to specify the gridded density field at $t = 0$ and the amplitudes of the Fourier components defining τ, B, ζ, p_ℓ, and ρ_b on the open boundaries. The control vector $\mathbf{C}$ is made up of the gridded initial density field and the amplitudes of the Fourier components. The maximum length of $\mathbf{C}$, corresponding to the maximum $L = 7$ used the present study (see (1)), was 14,007. The total number of data points, including the "bogus data" [see Thacker, 1988] from the regularization terms, is 91,767. Consequently, there are 91,767/14,007 ~ 6.5 data points per control variable on average and the underlying nonlinear regression problem of estimating $\mathbf{C}$ can be considered well posed if we assume that the data are dynamically independent.

The first guess for the ocean state was obtained by integrating the model for 1 year, initialized by the observed January density field and with first guesses for all model parameters and boundary conditions. The first-guess boundary conditions were obtained directly from the observations. The cost function was minimized iteratively using the so-called adjoint method [e.g., Le Dimet and Talagrand, 1986].
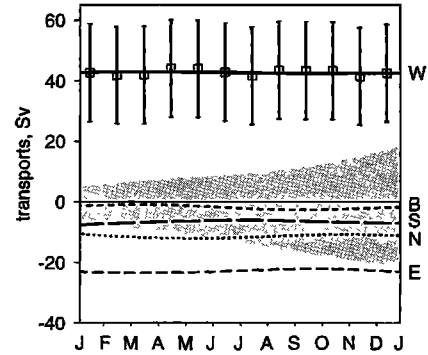

Figure 5. Transport through the model boundaries according to the dynamical method and the model run without data assimilation. The squares show estimates for the western boundary transport based on the surface-referenced dynamical method. The vertical lines show their standard errors. The remaining lines show transports estimated in experiment A0. The shaded area shows the standard error for the estimated vertical transport through the bottom boundary.

4. Estimated State of the North Atlantic

We now describe results from the dynamical method and the prognostic model integrated with and without data assimilation. To assess the fit of the model, we introduce two more standard deviations. The standard deviation of the difference in the monthly observations and the corresponding model prediction is denoted by σ_{md}. The standard deviation of our estimate of the ocean state is denoted by σ_p. It is obtained from the shape of the cost function in the vicinity of the minimum. To obtain an explicit expression for σ_p, consider the simplest case of a linear model that maps the controls $\mathbf{C}$ onto the model state $\mathbf{X}$, $\mathbf{X} = \mathcal{A}\mathbf{C}$. The dynamic method fits into this category. Let $\mathbf{Y}$ denote the observation vector. It is related to the true ocean state by $\mathbf{Y} = \mathcal{A}\mathbf{C} + \varepsilon$, where ε is a random error with zero mean and covariance Σ. The generalized least squares estimate for $\mathbf{C}$ is $(\mathcal{A}'\Sigma^{-1}\mathcal{A})^{-1}\mathcal{A}'\Sigma^{-1}\mathbf{Y}$, and the estimate for the true ocean state is $\mathcal{A}(\mathcal{A}'\Sigma^{-1}\mathcal{A})^{-1}\mathcal{A}'\Sigma^{-1}\mathbf{Y}$. This estimator has covariance $\Sigma_p = \mathcal{A}(\mathcal{A}'\Sigma^{-1}\mathcal{A})^{-1}\mathcal{A}'$. Prior to the regression, confidence intervals for $\mathbf{C}$ would be based on the diagonal elements of Σ. After the regression the confidence intervals are based on the (generally smaller) diagonal elements of Σ_p. The diagonal elements of Σ_p are sometimes referred to as posterior error variances (σ_p^2). Confidence interval based on the posterior variances are sometimes referred to as posterior confidence intervals. These ideas generalize in a fairly straightforward way to nonlinear models and were recently implemented in practice by Gunson and Malanotte-Rizzoli [1996] and Yaremchuk et al. [1998].

4.1. Dynamic Method

The dynamic method with the reference surface flow set by TOPEX/Poseidon data gives a mean transport through the western boundary of 43 Sv (Figure 5). The compensating outflows through the north, south, and east boundaries are 11, 8, and 23 Sv. We will summarize these transports in the form (43W, 11N, 8S, 23E). The error bars on the annual means are a few sverdrups, certainly much less than the errors bars on the monthly estimates, which are of order 15 Sv (Figure 5). The main contributor to the uncertainty in the estimates can be traced back to the prior error variances of the altimeter data.
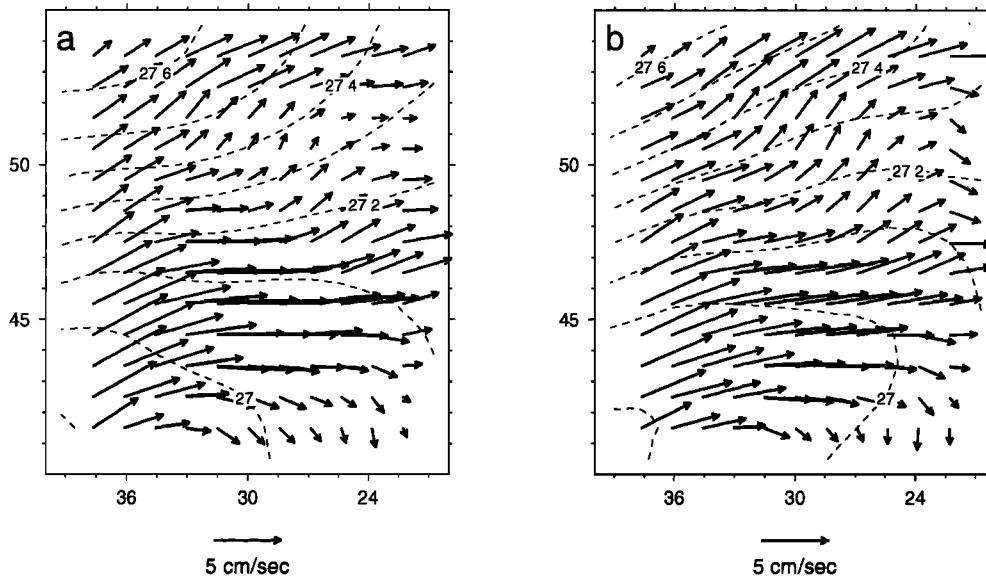
Figure 6. Annual mean geostrophic velocity and density at 400 m. Computed using (a) the surface-referenced dynamical method and (b) the prognostic model without data assimilation, experiment A0.

Dietrich et al.'s [1975] classic scheme of the circulation of the top 1000 m of the North Atlantic can be summarized for our domain as follows: (39W, 15N, 10S, 14E). We estimate the error bars to be between 5 and 8 Sv. *Dietrich et al.'s* [1975] values are quite close to those predicted by the surface-referenced dynamic method. If we assume a level of no motion at 1000 m, the corresponding transport predictions from the dynamic method are (23W, 8N, 5S, 10E). These are considerably weaker than the other two estimates, pointing to the importance of allowing for horizontal flows at 1000 m depth.

Net vertical transport through the bottom boundary is downward at rates of 2.2 and 1.3 Sv for the dynamic method based on a surface reference and a level of no motion at 1000 m, respectively. Both estimates are in reasonable agreement with the climatological mean vertical velocity presented by *Arhan et al.* [1989]. They also agree in sign with the North Atlantic inversion pattern of *Martel and Wunsch* [1993], who obtained a net downwelling of about 1 Sv at 1100 dbar.

4.2. Prognostic Model Without Data Assimilation

The velocity field calculated using the dynamical method is inconsistent with the density field in that the diapycnal flow is unrealistically large (note large angles between the density contours and inflow velocity vectors in Figure 6a). One way to overcome this deficiency is to run the prognostic model with the initial conditions and boundary conditions estimated directly from the observations (experiment A0, Table 1).

Horizontal transports are not strongly affected by allowing the density field to evolve with the flow. The reason is that these transports are determined primarily by the lateral boundary data, which are held fixed. On the other hand, transport across the lower boundary does depend on the interior density field (Figure 5). The prognostic run predicts convergent horizontal motion throughout the year, leading to an annual mean transport through the bottom boundary of 2.2 Sv. The maximum vertical transport is predicted for fall; however, this seasonal variation cannot be regarded as statistically significant given the size of the error bars in Figure 5, which grow with time.

Although the velocity fields from experiment A0 are more closely aligned with isopycnals than are results from the dynamic method (compare Figures 5a and 6b), this experiment fails in other respects. For example it fails to capture the seasonal variation of density over the top 400 m, in particular, the pronounced minimum in late summer (Figure 2). The model also gives a density field that moves well beyond the error bars of the density data (σ_d) after a couple of months of model integration. (See the thin lines in Figure 7a without shading.) Given the deficiencies of experiment A0, we now move to a data assimilative form of our circulation model in which the initial conditions and boundary conditions are systematically adjusted to bring the model predictions in line with the observations.

4.3. Prognostic Model With Data Assimilation

We will now focus on experiment A1 (Table 2). A mean and annual cycle were used to describe the temporal variation of the controls $(L = 3$ in (1)), and instabilities in the water column were removed using conventional hydrostatic adjustment. Additional information including parameter settings is given in Table 2.

4.3.1. Volume transports. The annual mean transport through the western boundary is 51.4 ± 2.6 Sv (Figure 8). It is compensated by outflows of 16.2 ± 1.8, 5.2 ± 2.4, and 28.2 ± 1.9 Sv through the north, south, and east boundaries, respectively. These transports are about 20% larger than the results of the surface-referenced dynamical method for all boundaries except the south. This is consistent with more recent studies [*Krauss et al.*, 1987; *Sy*, 1988], which find more intense easterly currents and no permanent recirculatory branch to the south.

Experiment A1 is in reasonable agreement with a recent estimate of the transport through a standard meridional section along approximately 27°W between 40° and 52°N [*Sy et al.*, 1992]. Mostly on the basis of hydrographical data, Sy et al. calculate a transport of 30 ± 9 Sv, close to the prediction of 36 ± 4.5 Sv from experiment A1.

The seasonal range in transport through the western boundary is 19 Sv with extremal values of 61 ± 5.1 and 42 ± 5.3 Sv
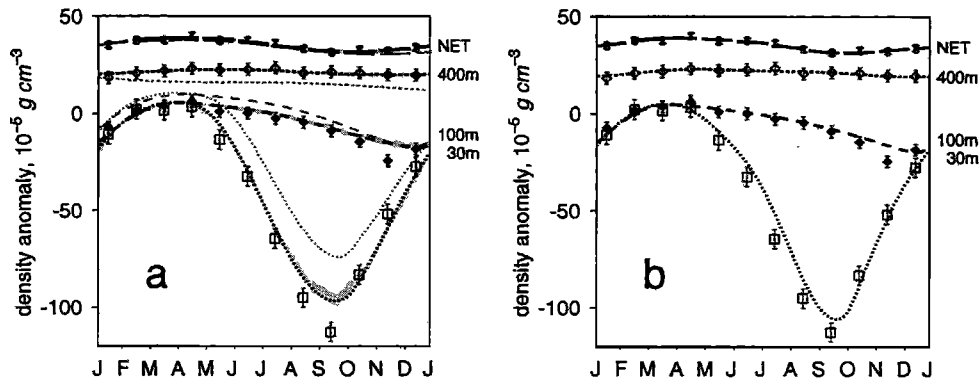
Figure 7. Comparison of observed and predicted density at various levels: (a) experiment A1 and (b) experiment B3. The symbols show the monthly means of observed density averaged across the domain at depths of 30, 100, and 400 m and over the top 1000 m. The vertical lines show the standard errors. The thin lines are predictions from experiment A0 (no data assimilation). The thicker lines in Figures 7a and 7b refer to experiment A1 and experiment B3, respectively. The shaded areas around the curves show the standard error of the estimate from experiment A1.

in May and November, respectively (Figure 8). Approximately 80% of this 19 Sv seasonal variation can be balanced by outflow through the southern boundary. The predicted autumnal inflow through the southern boundary cannot be considered reliable given its standard errors (see shaded areas of Figure 8a). The eastern outflow ranges between 32 ± 4 and 25 ± 3.9 Sv from April to October. This seasonal variation can be balanced by outflow through the northern boundary, which reaches extremal values of 22.5 ± 3.6 and 10 ± 3.7 Sv in September and February, respectively.

Seasonal variability of the North Atlantic Current is not well described in the literature. There is an indication in the work of *Baryshevskaya* [1985], based on repeated hydrological sections, that the NAC transport is stronger in summer than in fall. However, these transports should be interpreted really as circulation snapshots rather than as climatological means.

The annual mean transport through the bottom boundary is downward at a rate of 1.8 ± 0.4 Sv (Figure 8a). Downwelling prevails from April through November, with a maximum of 3.8 ± 0.7 Sv in July. Upwelling is predicted for the rest of the year, although the standard error on this prediction suggests that the upwelling is not significantly different from zero. The mean downwelling is in reasonable agreement with results of *Arhan* [1990] and the inverse calculation of *Martel and Wunsch*

[1993], which gives downwelling of ~1 Sv at the 1100 dbar level. On average, only 30% of the vertical transport is due to Ekman pumping. The rest is caused by large-scale flow convergences due to the β effect.

4.3.2. Density. Density variations from experiment A1 match the observations more closely than do variations from experiment A0 (Figure 7). The asymmetry in the seasonal cycle is the result of convection, which deepens the upper mixed layer to 100 m in winter. Overall, the error bars of the observations and model estimates overlap. The main exceptions are found in September at 30 m and in November at 100 m. These discrepancies can be reduced, but not eliminated, by better temporal resolution (higher L) of the boundary forcing (Figure 7). Even with the better resolution, the model fails to capture the abrupt transition of upper layer density when heating switches to cooling. During this transition the stratification is still stable, and so, the discrepancy is probably not due to the convection scheme. We attribute the discrepancy to the fact that we have not explicitly allowed for the stronger wind-driven turbulent mixing at this time of year.

The standard errors of the estimated density are about 20–25% that of σ_d (Figure 9). However, the ratio grows with time to the point that it is 35–40% that of σ_d by the end of the year. This error growth reflects the limited controllability of the
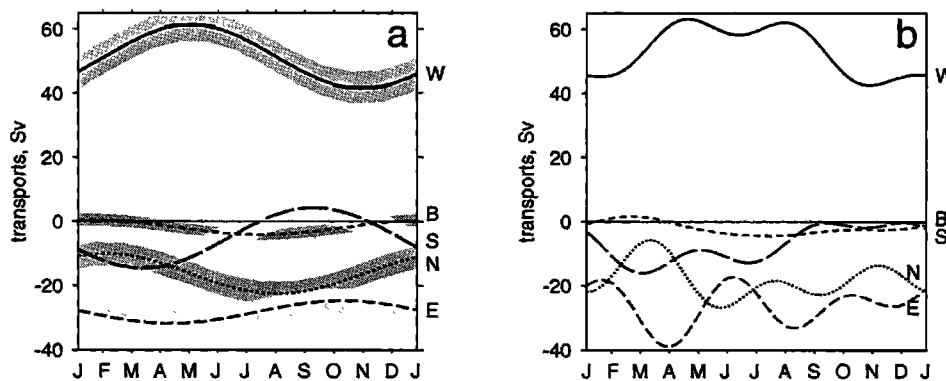

Figure 8. Volume transport through the open boundaries of the domain: (a) experiment A1 and (b) experiment B3. Curves labeled W, E, S, N, and B refer to the west, east, south, north, and bottom boundaries, respectively. The shaded areas in the left panel show the standard errors of the estimate.
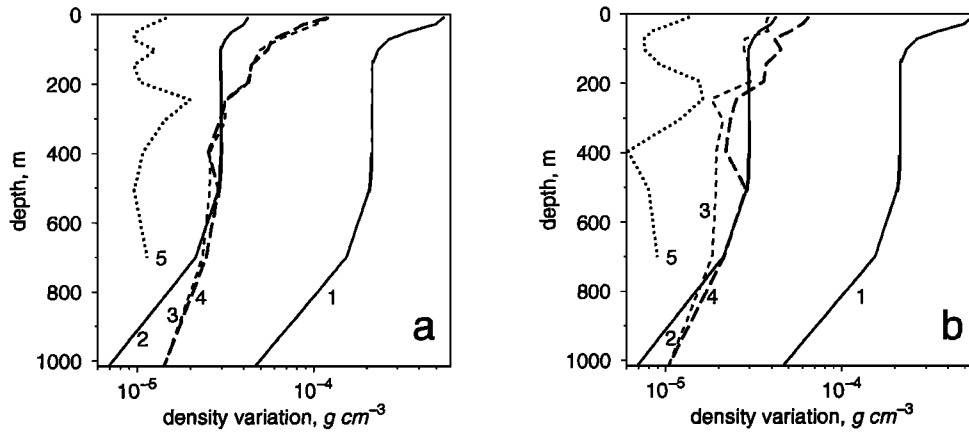
Figure 9. Standard deviation of density as a function of depth: (a) experiment A1 and (b) experiment B3. The solid curves labeled 1 show σ_{obs}, the standard deviation of the observations obtained by averaging horizontally at the depth specified over 1 year. The solid curves labeled 2 show σ_d, the standard error of the observations. Curves 1 and 2 are the same in both Figures 9a and 9b. The dashed lines labeled 3 and 4 show σ_{mod}, the standard deviation of the error in representing the observations by a best fitting mean and annual cycle, and σ_{md}, the standard deviation of the difference between the model solution and observations, respectively. The dotted curve labeled 5 shows the standard deviation of the annual buoyancy trend, $\sigma_{\rho_0 - \rho_T}$, obtained by averaging horizontally the mean square difference between density at the beginning and end of the 1 year integration.

model by the initial conditions and boundary conditions. One source of the error growth is probably the loss of information during convective adjustment (see Appendixes A and B), but other sources related to the strong nonlinearity of the model may also be important. Figure 9 also suggests that we may have underestimated the standard error of the observed densities at 1000 m by a factor of 1.5. Even with a temporal resolution of 2 months ($L = 7$), we find that σ_{mod} and σ_{md} exceed σ_d. Short-period variations, which cannot be modeled by the present system of equations, may be affecting the climatological density observations and should be treated as an additional source of observational noise.

The annual trend of density, measured by the standard deviation of its change over the integration interval of 1 year ($\sigma^S_{\rho(T) - \rho(0)}$), is comparable to its prior error estimate of 2×10^{-5} g cm^{-3} yr^{-1} (Table 1). It is clear from Figure 9 (curves labeled 5) that $\sigma^S_{\rho(T) - \rho(0)}$ does not depend strongly on the temporal resolution of boundary forcing. It is also relatively constant. The spatially averaged value of $\rho(T) - \rho(0)$ changes from positive in the upper 100 m, to negative between 100 and 350 m, and then to positive from 350 to almost 600 m. Below 700 m the trend is small, probably because the lower boundary of the model at 1000 m has strictly periodic boundary conditions. The net annual trend of density field is $<10^{-5}$ g cm^{-3} yr^{-1} and can be considered negligible.

4.3.3. Currents. The annual mean velocity at 350 and 600 m is nearly parallel to the isopycnals (Figure 10). The flow also shows a slight clockwise rotation with depth in agreement with the sign of the β spiral in the subpolar gyre [*Stommel and Schott*, 1977]. The standard errors on these annual mean velocities are about 0.2–0.3 cm s^{-1}.

The open arrows in Figure 10 are velocities obtained by averaging over clusters of long-term current meter measurements [*Arhan et al.*, 1989]. Error bars for these mean velocities were calculated using the variance and decorrelation time of the observed velocities. (The decorrelation time was estimated to be 10 days [*Arhan et al.*, 1989].) The length of the current

records ranged from 1 (cluster C at 350 m) to 4.34 years (cluster A at 350 m). The error bars are about 4 cm s^{-1}, more than a factor of 10 larger than the standard errors on the annual mean from experiment A1.

The agreement between the observed and estimated currents at 350 m is reasonable at locations A, B, and D, with the estimated mean flow falling inside the confidence regions around the mean of the observations. Given the size of the error bars, all that the observations really tell us is that the overall flow is eastward at speed of about 5 cm s^{-1}. The agreement at location C is poor, but we note that the mean of the observations at this location is anomalous compared to the other observations. It would appear that averaging over 1 year is not enough to obtain a good estimate of the mean flow in this region. (The observed flow at location C was excluded from the analysis presented by *Arhan et al.* [1989].) The observed and estimated mean flow at 600 m is weaker than the flow at 350 m with a speed of about 3 cm s^{-1}. Although the estimated means almost fall within the confidence regions around the observed means we note, but cannot explain, a direction bias with the observed flow having a stronger southward component.

Brügge [1995] has mapped the mean North Atlantic circulation on the basis of ~200 drifting buoy trajectories drogued at 100 m and deployed in the Gulf Stream region over the period 1981–1989 (Figure 11). Velocities were calculated from the trajectories and averaged in 3° × 2° bins. The typical number of observations per bin in the present study region is about 200 buoy days. However, the number of observations per bin is not uniform; it varies from a maximum of about 300 buoy days in the southwest corner to almost zero along the northern boundary. *Brügge* [1995] assumed a relatively low error standard deviation of 1 cm s^{-1} for the mean bin velocities. It is hard to rely on this error estimate because, as we saw for the current meter data set described by *Arhan et al.* [1989], even a 4 year averaging interval is barely sufficient to provide a reasonable estimate of the mean given the strong mesoscale variability in this region.
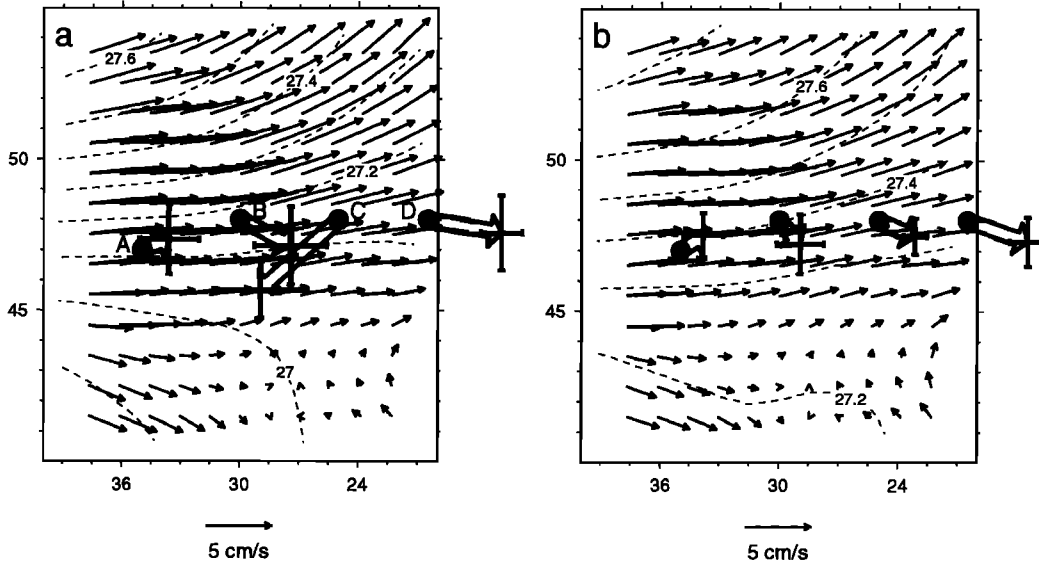
Figure 10. Annual mean velocity and density from experiment A1 and current meter observations from *Arhan et al.* [1989] for (a) 350 and (b) 600 m depth. The crosses at the end of the observed current vectors show the error bars calculated by *Arhan et al.* [1989].

The annual mean velocity at 100 m from experiment A1 has one feature in common with the observed map of *Brügge* [1995]: weak and randomly oriented currents south of 45°N (Figure 11). North to 45°N, the directions of the two patterns agree reasonably well, with almost zonal flow in the area where NAC enters the region to about 30°W. Farther east, we can identify a branch associated with the subarctic front that turns to the northeast (north of 50°N). The observed speeds are about 50% higher than the predictions from experiment A1. The discrepancy is strongest near the inflow region and the northeast branch. The discrepancy may be due to the heavy smoothing used to produce the Levitus climatology.

Standard errors of the horizontal and vertical velocities estimated by experiment A1 range between 0.2–0.3 cm s^{-1} and 7–15 m yr^{-1}, respectively. Error bars for horizontal velocities

do not exceed 10–20% of their amplitudes, which allows us to identify them as reliable.

4.3.4. Surface forcing. The sea level field predicted by experiment A1 has the same meridional drop as the TOPEX/Poseidon observations (Figure 12). However, the predicted sea level has a sharper meridional gradient north of 45°N than the observations, suggesting a transition between a well-defined NAC and a more southerly region with weak mean flow. This is in agreement with the works of *Sy* [1988], *Arhan* [1990], and *Sy et al.* [1992] that indicate no permanent branches of the NAC system south of 45°N. This current intensification was a persistent feature in all of our experiments except those with steady boundary conditions or without parameterization of the upper mixed layer.

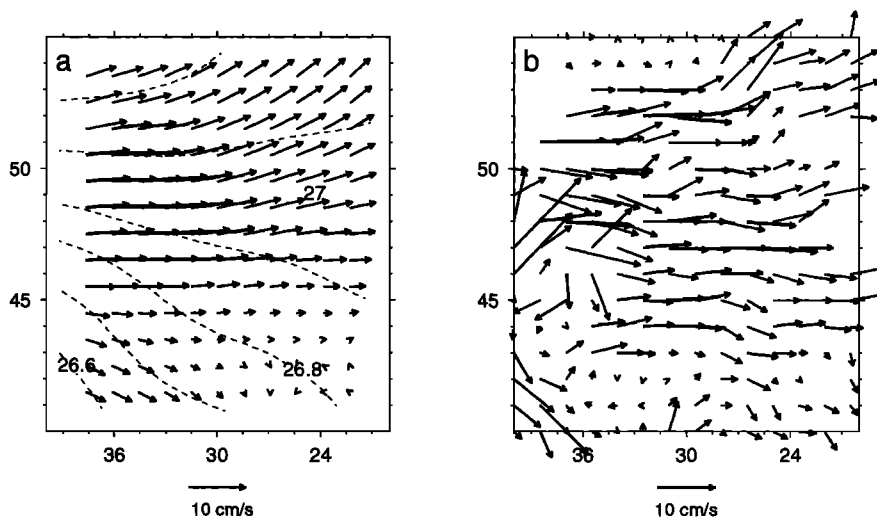The observed and estimated wind stress fields are in good

Figure 11. Annual mean velocity and density at 100 m from (a) experiment A1 and (b) the mean (nondivergent) velocity derived from drifting buoys by *Brügge* [1995].
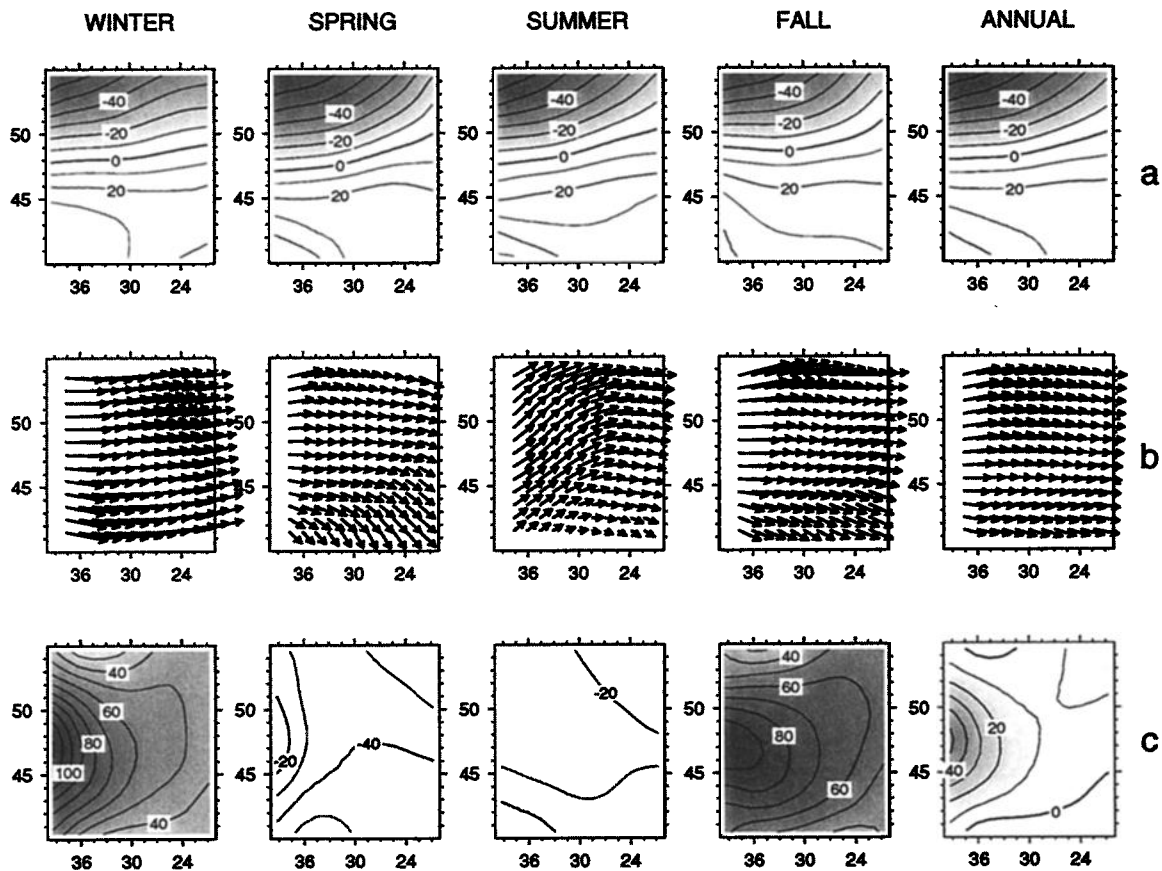
Figure 12. Estimated surface conditions from experiment A1: (a) sea level in cm, (b) wind stress, and (c) buoyancy fluxes in 10^{-8} g cm^2 s^{-1}.

agreement (Figure 12). Differences generally do not exceed 0.15 cm^2 s^{-2} and are well within the standard error of the observations (Table 1).

The surface buoyancy fluxes predicted by experiment A1 differ from observations in a couple of ways (Figure 12). First, the fall-winter surface cooling associated with NAC extends farther east in the predictions. Second, the predicted buoyancy flux is more spatially uniform than the observations in summer. In particular, the hint of a buoyancy flux anomaly associated with advection of warm surface water by NAC is evident in the summer observations but not in the optimal state.

Standard errors of the estimated atmospheric forcing and sea level are given in Table 1. Encouragingly, the discrepancies between model and data (measured by σ_{md}) are smaller than, or close to, errors in representing the data by a mean and annual cycle (σ_{mod}). Exceptions are the surface buoyancy flux and sea surface elevation. Overall, the posterior errors σ_p for density are 2–4 times smaller than the prior error σ_d. Overall, these figures indicate that our model is consistent with the assumptions about the statistics of measured buoyancy, wind stress, and sea level.

5. Robustness of the Assimilation Solution

We now examine the sensitivity of the assimilation results to changes in the underlying dynamics and the parameters in the cost function. The numerical experiments discussed in the rest of this section are listed in Table 2. Experiments B1–B3 examine the sensitivity to the temporal resolution of the boundary

forcing. For example, experiment B2 allows for annual and semiannual components ($L = 5$). Experiments C1–C4 examine the effect of changing the horizontal (A_l) and vertical (A_{v0}) diffusivity. Experiments E1 and E2 examine the effect of changing the type of convective parameterization. Experiment E1 is an extreme case in which convection is turned off in the model.

5.1. Temporal Resolution of Boundary Forcing

In experiment B1 the temporal variability in the boundary forcing is suppressed ($L = 1$). Not surprisingly, the model-data misfits generally exceed the assumed noise levels of the monthly means of observations (Table 3). Steady forcing also tends to produce negative mean surface buoyancy fluxes (i.e., excessive heating through the surface). *Marotzke and Wunsch* [1993] and *Nechaev et al.* [1995] obtained similar results in their attempt to model the steady state North Atlantic using similar equations. Finally, the suppression of the seasonal changes in boundary forcing has a significant effect on the mean transport through the western boundary: it drops from 51 to 41 Sv (Table 4).

Higher temporal resolution of the controls generally produces better fits of the model to the observations (Table 3). For example, Figure 7b shows the result of increasing L from 3 to 7 (experiment B3; see Table 2). The model error σ_{mod} is now generally smaller than σ_d, and σ_{md} is reduced. Overall, the results experiments A1, B2, and B3 are qualitatively similar. To illustrate we summarize the volume and buoyancy transports through the western boundary of the model domain in Table 4.

Table 3. Effect of Temporal Resolution of the Boundary Forcing on σ_{md}, the Standard Deviation of the Difference Between the Monthly Observations and Model Predictions

| Experiment | L^a | Density, ρ | | | | B | ζ | τ | $\Delta\rho$ |
		30 m	100 m	400 m	1000 m				
B1	1	40.	10.	3.1	1.5	54.	6.7	0.44	2.0
A1	3	8.7	5.5	2.5	1.4	14.	7.1	0.35	1.2
B2	5	6.5	4.6	2.3	1.2	17.	7.6	0.25	1.2
B3	7	5.9	4.5	2.2	1.0	16.	8.0	0.22	1.0

[a]L is the number of terms in the Fourier representation of the boundary forcing. Otherwise definitions and units are the same as in Table 1.

The transports from B2 and B3 fall within the standard errors of the estimate from experiment A1. Consider now the vertical structure of the density errors from experiment A1 in more detail. Figure 9a shows that σ_{mod} exceeds σ_d for depths above 200 and below 700 m. This results from the relatively low temporal resolution of the boundary forcing ($L = 3$) used in experiment A1.

5.2. Diffusion Coefficients

The region under consideration is characterized by high levels of eddy kinetic energy that are expected to affect strongly the large-scale circulation. Eddy effects in the model have been parameterized by harmonic diffusion. We recognize that the application of such a simple parameterization to geostrophic turbulence is uncertain.

We varied the horizontal diffusivity coefficient A_l between 2 and 40×10^6 cm^2 s^{-1} in experiments C1–C3. Experiment A1, the base run, had a diffusivity of 20×10^6 cm^2 s^{-1}. Over the range 2 to 10×10^6 cm^2 s^{-1} the optimal state did not change significantly with A_l. However, as A_l increased from 10 to 40×10^6 cm^2 s^{-1}, the annual mean transport and buoyancy fluxes through the western boundary dropped by ~10%. Simultaneously, the eastern outflow transport grew, and the northern and southern outflows weakened. The increased horizontal diffusive flux of relatively dense water into the model domain with higher A_l is partially compensated by stronger advective loss through the bottom boundary.

It is possible that eddy transports of buoyancy are more efficient than the diffusive fluxes obtained by conventional parameterization used in experiment C3. It is also possible that turbulent buoyancy fluxes are proportional to the large-scale buoyancy field instead of its gradient. If this is the case, optimal velocity fields obtained from buoyancy conservation may contain a component (the so-called bolus velocity [Gent et al., 1995]) parameterizing the corresponding Reynolds fluxes in the large-scale buoyancy balance. Comparison of experiments A1 and C1–C3 provides a sensitivity estimate to the rate of buoyancy diffusion. It may also give a very rough idea of the amplitude of the bolus velocity. Let us assume that the param-

eterization of diffusion in experiment A1 underestimates the turbulent buoyancy fluxes by an order of magnitude and that these fluxes that are required to balance the buoyancy budget are compensated in experiment A1 by an additional (bolus) velocity field. The comparison of experiments A1 and C3 suggests that if turbulent buoyancy fluxes are 10 times higher, the volume transports should be ~30% smaller. This 30% difference in volume transports could be attributed to the impact of bolus velocity transports.

Assuming a typical geostrophic turbulent length scale of $l = 20$ km and eddy kinetic energy of $E \sim 200$ cm^2 s^{-2} [Brügge, 1995] gives an eddy diffusivity of $A_l \sim l\sqrt{E} \sim 28 \times 10^6$ cm^2 s^{-1}. The lower value of 20×10^6 cm^2 s^{-1} used in experiment A1 is a compromise between the inadequacy in our geostrophic turbulence parameterization and results from the above simple-scale analysis. As we have shown in experiments A1 and C1–C3, values of A_l larger than 20×10^6 cm^2 s^{-1} begin to have an effect on the circulation. This effect may be inconsistent with physical reality because of the inadequacy of the parameterization scheme [e.g., Tai and White, 1990; Brügge, 1995].

For experiment C4 we doubled the vertical diffusivity used in experiment A1. The only change in the ocean state was a slight (10%) weakening of the eastern outflow in favor of the southern outflow. This redistribution is associated with a small (3°) northward shift of the entire circulation pattern. The southern outflow grows to 18 Sv in March (compared to 14.5 Sv in experiment A1), but the amplitude of the seasonal changes remains unchanged.

5.3. Convective Adjustment

Two upper mixed layer parameterizations, namely, conventional hydrostatic adjustment (experiment A1) and nonlinear vertical diffusion (experiment E2), are now compared against a run without convective adjustment (experiment E1). Experiment E2 produces a circulation pattern that is qualitatively similar to that of experiment A1. The main disadvantages of the nonlinear diffusion parameterization used in experiment E2 are that it leads to a poorer (by about 20%) fit to the upper ocean density data and can allow unstable density profiles.

Table 4. Effect of Temporal Resolution of the Boundary Forcing on the Transports Through the Western Boundary of the Model Domain[a]

Experiment	L	Annual	Winter	Spring	Summer	Fall
B1	1	41.0				
A1	3	51.4 ± 2.6	53.7 ± 4.1	60.1 ± 4.1	49.2 ± 3.8	42.8 ± 3.7
B2	5	52.8	53.5	58.8	54.4	44.6
B3	7	53.3	50.3	60.6	57.7	44.4

[a]Transports are in sverdrups.

The nonconvective solution from experiment E1 does not lie within the error bars of the data. The model-data misfit exceeds the confidence limits of both the density and the surface buoyancy flux data. The circulation pattern obtained from this experiment does not agree with the other experiments. In particular, the western inflow reaches a maximum of 60 Sv in January, which is compensated mainly by outflow through the southern boundary (55 Sv).

To summarize this section, we conclude that model is robust to moderate variations in the means and variances of the observations. We also showed the importance of (1) resolving the annual cycle of the forcing and (2) parameterizing the winter convection. Ignoring these features leads to qualitatively different oceanic states resulting from assimilation of the same data set.

6. Discussion

A dynamically consistent estimate of the large-scale circulation of the open North Atlantic has been obtained by combining a variety of climatological data sets. The combination of simplified dynamics and a relatively large amount of data (43,000 data points) led to an inversion problem that is rather well conditioned apart from some loss of controllability associated with winter convection.

The choice of a model domain with all boundaries open has one important advantage over models with coastlines: it was not necessary to model the complicated boundary layer dynamics. This is important from an assimilation perspective because an accurate representation of the boundary layer would require a higher-resolution model than the one used in the present study. This, in turn, would lead to a reduction in the ratio of data points to controls and a deterioration in the conditioning of the inversion problem. The simplified dynamics used in this study apply to a relatively narrow spectral band of motions (300–1000 km and 30–300 days), which are driven mainly by the open boundary forcing. In this sense our results are diagnostic in character; with the present model it is not possible to identify unambiguously the physical origin of much of the variability in the gyre-scale dynamics.

The relatively low dimension of the control space enabled us to perform a fairly complete posterior error analysis. This type of analysis is rarely seen in the literature on variational data assimilation. As well as allowing us to construct error bars for the estimated state, this analysis allowed us to examine the multivariate covariance structure of the estimated state and its forcing (see Appendix B). The consideration of the posterior cross correlations between the key characteristics of the optimal state (Appendix B) supported the governing role of boundary transports in the seasonal variation of the circulation in the region.

The study has been focused on obtaining statistically and dynamically consistent estimates of the transports and fluxes associated with the NAC and their seasonal variability. By utilizing a 4-D variational approach we have obtained new estimates of the net horizontal and vertical transports and buoyancy fluxes, which were supplied by rigid error bars derived from dynamically consistent error analysis of the optimized state. These estimates are free of ad hoc assumptions on the horizontal structure of level of no motion and cannot be obtained from the purely statistical analysis of the data. It has been also shown that traditional schemes of data processing (like the dynamical method referred to observed sea surface topography or direct model integration with "climatological" boundary conditions) produce more indefinite results owing to statistical and/or dynamical inconsistency of these algorithms.

Some of the more quantitative conclusions of the present study are as follows.

1. Assuming a level of no motion at 1000 m in the study area is incorrect, leading to a significant underestimation of the transport. For example, the NAC transport across 40°W is 23 Sv; using TOPEX/Poseidon data to fix the velocity at a surface reference level gives a transport of 43 Sv, a value much closer to the generally accepted rate.

2. The traditional dynamic method gives flow fields that are inconsistent with the Levitus [1994a, 1994b] and Levitus and Boyer [1994] climatology.

3. The volume transport of the upper 1000 m of the North Atlantic Current across 40°W between 40° and 55°N is 51 ± 3 Sv. This transport is subject to seasonal changes with a range of 19 Sv; the maximum transport of 61 ± 5 Sv is in April–May and the minimum of 42 ± 3 in October–November.

4. The western inflow is compensated by annual mean outflows of 28 ± 2 (east), 16 ± 2 (north), and 5 ± 2 Sv (south) and downwelling of 1.8 ± 0.4 Sv. The southern outflow has the largest seasonal variability, ranging from 14 Sv in March–April to −4 Sv in September–October. Upwelling through the bottom boundary is the least certain.

5. Horizontal advection is the major contributor to the local buoyancy budget: the excess of relatively light water $(10.9 \pm 1.5 \text{ kton s}^{-1})$ brought from the west is compensated by northern (7.7 ± 1.9), eastern (5.3 ± 1.3), and southern (1.4 ± 1.1) outflows. The net imbalance of the horizontal advective fluxes $(-0.7 \text{ kton s}^{-1})$ is balanced primarily by annual mean atmospheric cooling $(1.7 \text{ kton s}^{-1})$ and vertical advection through the bottom boundary $(-1.1 \text{ kton s}^{-1})$. Lateral buoyancy diffusion play a minor role. The horizontal advective divergence is especially pronounced in late summer and beginning of fall; it explains 40–50% of the temporal changes in the net buoyancy content.

6. Nonlinear effects are important in interpolating and smoothing the climatological data. With steady boundary conditions the annual mean transports are 15–25% smaller than the transports obtained with periodic forcing. Winter convection is also shown to play a significant role in setting the overall circulation pattern.

The volume transports given above are generally 10–20% larger than the values quoted in the literature. We attribute this to the fact that our model includes a prognostic density conservation constraint. The dynamical system compensates for the excess of negative buoyancy input from atmosphere through a divergence of the horizontal transport, thereby adjusting the geostrophic velocity field. We suggest that this correction may reflect the impact of the Reynolds fluxes divergences, which may be implicitly present in the time series of Levitus [1994a, 1994b] and Levitus and Boyer [1994] data and which are hardly captured by "standard" data analysis underlying most of the independent transport estimates known in literature. On the other hand, it is noteworthy that the drifter data analyzed by Brügge [1995] indicate larger transports than earlier estimates and are thus more in accord with our results. Note that the higher transports emerge only when the model state is optimized in its time-dependent, nonlinear mode (Table 4). In contrast to the steady state, where the buoyancy balance can be achieved at low transports and relatively high rates of nonadiabatic processes, the time-dependent mode im-

poses direct constraints on the magnitude of the velocity: water with different hydrodynamic properties cannot be formed inside the model domain but must be advected through its open boundaries. Thus the temporal derivatives of the density field combined with its characteristic spatial gradients prescribe the transports required to achieve the advective buoyancy balance by geostrophic velocities.

The annual mean buoyancy flux predicted in experiment A1 has a persistent large-scale bias with respect to the observations of about 10^{-7} g cm^{-2} s^{-1}. One of the reasons for that may be attributed to isobaric interpolation underlying the *Levitus* [1994a, 1994b] and *Levitus and Boyer* [1994] climatology. Horizontal averaging of the T/S properties of the migrating fronts of the upper layer may produce spurious water masses and bias the vertical gradients in the density field, causing inconsistency with the surface flux data. Another reason may be attributed to uncertainty in the climatological estimates of the fluxes of heat and fresh water. For example, it has been argued [e.g., *Arhan et al.*, 1989] that our study region has the largest excess of precipitation over evaporation in the North Atlantic. To study the sensitivity of our results to uncertainties in buoyancy forcing, we constructed "alternative" buoyancy forcing by adding spatially uniform and time-invariant fluxes of fresh water and heat of 25 cm yr^{-1} and 30 W m^{-2}, respectively, to B. The subsequent assimilation experiments showed that the corresponding optimal states were closer to each other than the buoyancy forcings, separated by the bias of 10^{-7} g cm^{-2} s^{-1}. We interpret this as an indication of the algorithm's ability to reduce the uncertainties of such a poorly observable parameter of large-scale ocean-atmosphere interaction as surface buoyancy flux.

Further developments of the present approach are worthy of consideration. For example, the model domain could be expanded to include the whole basin. Other tracer conservation constraints could be taken into the account to allow more data to be assimilated. Finally, the dynamics could be incorporated into the assimilation scheme as "weak" rather than "strong" constraints. This generalization would increase dramatically the dimension of the control space (of order 10^6 when considering global scales). However, the development of better numerical methods and faster computers will gradually make the solution of such large computational problems feasible, including the task of inverting a global oceanic data set like the one obtained in the World Ocean Circulation Experiment.

Appendix A

A standard way to parameterize convective adjustment is as a form of nonlinear diffusion:

$$\hat{\Pi}(\rho) = \mu \partial_z \theta (\rho_z) \partial_z \rho,$$

where

$$\theta[(\rho_z)] = \begin{cases} 0, & (\rho_z) \leq 0 \\ 1, & (\rho_z) > 0 \end{cases}$$

and μ is a positive constant that is sufficiently large to ensure that the convective relaxation timescale is much less than the timescales of the fastest processes resolved by the system. In the present study we used two finite difference approximation of $\hat{\Pi}$.

A1. Standard Second-Order Finite Difference Approximation

The condition $(\delta z)^2/\mu \gg \Delta t$ implies that the corresponding Courant-Friedrichs-Lewy number is much larger than unity. Since we used an implicit scheme for vertical processes, the major error in the approximation of $\hat{\Pi}$ is due to linearization within a single time step Δt. The impact of this error is negligible when density inversions are weak; that is, they do not generate secondary inversions after adjustment within the range of z for which $\partial_z \rho > 0$. We took $\mu = 0.04$ m^2 s^{-1}.

A2. Finite Difference Convective Adjustment

To avoid the linearization error mentioned above, the integration of $\rho_t = \hat{\Pi}(\rho)$ was represented in the form

$$\prod_{s=1}^{N(\rho)} \hat{\Pi}_{k(s)},$$

where $\hat{\Pi}_{k(s)}$ is an "elementary" mixing operator that performs mass-conserving averaging between layers ρ_k and ρ_{k+1}:

$$\hat{\Pi}_k = \begin{Vmatrix} 1 & 0 \\ 0 & 1 \end{Vmatrix} + \frac{1}{2} \theta (\Delta \rho_k) \begin{Vmatrix} -1 & 1 \\ 1 & -1 \end{Vmatrix}$$

and $N(\rho)$ is the total number of elementary mixing events necessary to transform a given profile $\{\rho_k | k = 1, \ldots, K\}$ into one with $\Delta \rho_k = \rho_k - \rho_{k+1} \leq 0$. (Note for simplicity we have assumed above that $\delta z_1 = \delta z_2 = \cdots \delta z_K$.) The tangent linear operator to $\hat{\Pi}_k$ is

$$\hat{\Pi}_k^t = \hat{\Pi}_k + \frac{1}{2} \Delta \rho_k \delta (\Delta \rho_k) \begin{Vmatrix} 1 & 0 \\ 0 & 1 \end{Vmatrix} = \hat{\Pi}_k.$$

We see that linearization of $\hat{\Pi}_k$ coincides with the operator itself. Therefore the adjoint finite different convective adjustment can be represented in the form

$$\prod_{s=N(\rho)}^{1} \hat{\Pi}_{k(s)}^T.$$

In practice, we have to store the space-time coordinates of all the elementary convective events that occurred during the forward run of the model and then apply their transposes (denoted by superscript T) in reverse order when running the adjoint code.

Appendix B

We now describe the calculation of the posterior error covariance of the ocean state estimated by experiment A1. It provides a measure of the changes in the estimated state that are to be expected as the observations change within their expected range of variability. More specifically, consider the ensemble of "data vectors" $\mathbf{d}$ and let $\mathcal{P}(\mathbf{d}) \sim \exp[-\mathcal{T}]$ denote their Gaussian probability distribution where $\mathcal{T}$ is the cost function. The estimated ocean state vector is a function of $\mathbf{d}$, and its second moments give us the posterior covariance structure and allow the construction of posterior error bars. Following the standard approach [*Thacker*, 1989], we assume that posterior statistics are also Gaussian and fluctuations around the optimal state are small in the sense that original dynamics is well approximated by linearized equations.

The posterior error analysis was the most computationally expensive part of the present study because it involved the

computation and inversion of the Hessian matrix as described below. All error calculations were performed in the vicinity of the optimal state from our base run, experiment A1 (see Table 1).

The Hessian matrix **H** was calculated by finite difference differentiating of the cost function gradient with respect to control variables. This operation required $N = 6033$ runs of the model and its adjoint. The spectrum of the Hessian matrix has a low-dimensional ($n = 429$) null space (Figure B1), and thus the Hessian cannot be inverted directly. Further investigation showed that this null space is due to winter convection, which causes loss of information on the vertical structure of the initial density field. In other words, the evolution of the oceanic state does not depend on the near-surface, vertical structure of the initial density distribution. To overcome this conditioning problem, we reduced the number of controls by replacing the controls describing the initial vertical density structure in the top four layers (0–75 m) by one control. With this modification the dimension of the new control space was reduced to $N' = 6033 - 429 = 5604$. The condition number of **H'** (Figure B1) is 32,000.

The next step was to invert **H'** using a standard routine from International Mathematics and Statistics Libraries, Inc. The covariance matrix between the control variables $\mathbf{K} = \mathbf{H'}^{-1}$ contains the information on the entire covariance structure of the optimal state.

B1. Variance Estimation

Variances σ_p of all quantities were computed through the linear transformations of the covariance matrix **K**. Let us consider as an example the algorithm for computation of the variance σ_p^2 for the volume transport through the eastern boundary of the domain for the month of April, $V_E^{m=4}$.

First, we compute the components of the vector **L**, which relates small fluctuations of control vector **C** around optimal value with a variation of $V_E^{m=4}$. This can be done using the adjoint code:

$$\mathbf{L} = \frac{\delta V_E^{m=4}}{\delta \mathbf{C}} = \mathscr{A}_{\text{opt}}^\dagger \frac{\delta}{\delta \mathbf{X}} \int_{S_E} \bar{u}^{m=4} \, dS,$$

where **X** is the state vector and $\mathscr{A}_{\text{opt}}^\dagger$ is the adjoint of the dynamical operator of the model in the vicinity of the optimal state. Then the variance can be calculated as
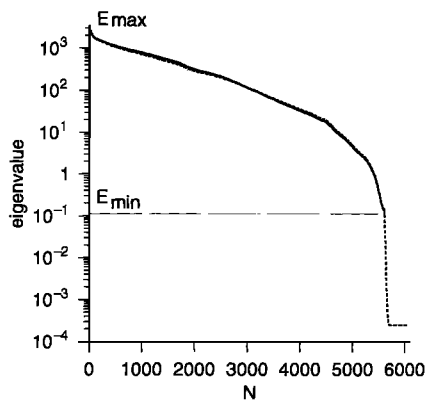

Figure B1. Spectra of the Hessian matrices $\bar{\mathbf{H}}$ (dashed curve) and $\bar{\mathbf{H}}'$ (solid curve) associated with assimilation scheme. See Appendix A for definitions of $\bar{\mathbf{H}}$ and $\bar{\mathbf{H}}'$.

$$\sigma_p^2(V_E^{m=4}) = L^T \mathbf{K} L.$$

B2. Cross-Correlation Analysis

Posterior probability distribution is defined (1) by the properties of our observing system and (2) by the structure of dynamical constraints. The observations are distributed homogeneously in time and space, and data errors are uncorrelated. Consequently, if we assume that the amount of utilized climatological data is adequate to resolve all the components of ocean state, cross correlations would be mainly induced by the dynamics. Therefore cross-correlation analysis might be useful to provide an insight of the physical processes governing circulation within model domain.

The covariance matrix **K** contains the full information on the cross correlations of the estimated state and its forcing, which is obviously redundant taking into account a certain freedom in our selection of the cost function. Therefore in the correlation analysis we consider a fixed set of integrals of the ocean fields, which is supposed to be less sensitive to uncertainties in the definition of the cost function. The analyzed set $\mathscr{I}$ of integral quantities characterizing the optimal state includes monthly mean transports of volume V and buoyancy V_p through the open boundaries of the box, monthly mean S-averaged values of wind stress τ, buoyancy flux B, and monthly mean S-averaged density values ρ at different levels in the vertical. Consequently, $\mathscr{I}$ is represented by $((2 \times 5 + 3 + 13) \times 12) = 312$-dimensional vector. The 312×312 covariance matrix **K'** was calculated through the linear transformation of the covariance matrix **K** in a way similar to obtaining σ_p^2.

Covariance matrix **K'** consists of the cells defined by the physical nature of their entries (e.g., cell $\tau - B$). The elements within the cells are ordered with month in columns and rows: the first element in the first column of $\tau - B$ cell is covariance of τ in January and B in January; the next element is covariance of τ in February and B in January, and so on. Correlation functions, extracted from the different diagonals of the corresponding cells in **K'**, are close to periodical and homogeneous in time. Deviations from homogeneity varied within 10–20% between different pairs of $\mathscr{I}$ components having significant correlations.

The transports of volume and buoyancy through lateral and lower boundaries demonstrate highest correlations. The corresponding temporal correlation functions do not demonstrate any significant (larger than a month) time shifts. Correlations with atmospheric buoyancy flux are much smaller in magnitude and have significant values for the components $\rho(0-100m)$, $V_{B,E,S}$, and $V_{B,E,S}^\rho$. Correlation functions $B - V_p$ demonstrate minimum in winter and low maximum in summer for the outflows at the bottom and eastern boundaries of the domain. In contrast, southern outflow is positively correlated with surface buoyancy flux, exhibiting stronger correlations in winter. Wind forcing appears to have a significant correlations only with the transports through the southern boundary. Stronger zonal winds in winter tend to export a considerable amount of cold water southward within the surface Ekman layer, explaining to some extent the above mentioned behavior of the $\tau - V_p$ and $B - V_p$ correlation functions.

From the general viewpoint we may assume that seasonal variability is caused by oscillations in the dynamics of the Subpolar Gyre as a whole, and therefore locally, the main driving forces are the lateral and lower boundaries. This gives some explanation why open boundary transports have been found to be correlated between each other and more weakly

correlated with "more independent" forcing coming from the atmosphere.

References

Arhan, M., The North Atlantic Current and Sub-arctic Intermediate Water, *J. Mar. Res.*, *48*, 109–144, 1990.

Arhan, M., A. C. de Verdiere, and H. Mercier, Direct observations of the mean circulation at 48°N in the North Atlantic, *J. Phys. Oceanogr.*, *19*, 161–181, 1989.

Baryshevskaya, G., Variability of discharge in the central North Atlantic Current, *Meteorol. Gidrol.*, *2*, 77–83, 1985.

Brugge, B., Near-surface mean circulation and kinetic energy in the central North Atlantic from drifter data, *J. Geophys. Res.*, *100*, 20,543–20,554, 1995.

Dietrich, G., K. Kalle, W. Krauss, and G. Sielder, *General Oceanography*, 626 pp., John Wiley, New York, 1975.

Fofonoff, N. P., and R. C. Millard Jr., Algorithms for computation of fundamental properties of seawater, *UNESCO Tech. Pap. Mar. Sci.*, *44*, 53 pp., 1983.

Gent, P. R., J. Willebrand, T. J. McDougall, and J. C. McWilliams, Parameterizing eddy-induced tracer transports in ocean circulation models, *J. Phys. Oceanogr.*, *25*, 463–474, 1995.

Gunson, J. R., and P. Malanotte-Rizzoli, Assimilation studies of the open ocean flows, 2, Error measures with strongly non-linear dynamics, *J. Geophys. Res.*, *101*, 28,473–28,488, 1996.

Isemer, H. J., and L. Hasse, *The Bunker Climate Atlas of the North Atlantic Ocean*, vol. 2, *Air-Sea Interactions*, Springer-Verlag, New York, 1987.

Isemer, H. J., J. Willebrand, and L. Hasse, Fine adjustment of large scale air-sea energy flux parameterization by a direct estimate of ocean heat transport, *J. Clim.*, *2*, 1173–1184, 1989.

Krauss, W., The North Atlantic Current, *J. Geophys. Res.*, *91*, 5061–5074, 1986.

Krauss, W., E. Fahrbach, A. Aitsam, J. Elken, and P. Koske, The North Atlantic Current and its associated eddy field southeast of Flemish Cap, *Deep Sea Res., Part A*, *34*, 1163–1185, 1987.

Krauss, W., R. H. Kase, and H. H. Henrichsen, The branching of the Gulf Stream southeast of the Grnad Banks, *J. Geophys. Res.*, *95*, 13,089–13,103, 1990.

Le Dimet, F. X., and O. Talagrand, Variational algorithms for analysis and assimilation of meteorological observations: Theoretical aspects, *Tellus, Ser. A*, *38*, 97–110, 1986.

Levitus, S., and T. P. Boyer, *World Ocean Atlas 1994*, vol. 4, *Temperature, NOAA Atlas NESDIS*, vol. 4, 129 pp., Natl. Oceanic and Atmos. Admin., Silver Spring, Md., 1994.

Levitus, S., R. Burgett, and T. P. Boyer, *World Ocean Atlas 1994*, vol. 3, *Salinity, NOAA Atlas NESDIS*, vol. 3, 111 pp., Natl. Oceanic and Atmos. Admin., Silver Spring, Md., 1994a.

Levitus S., T. P. Boyer, and J. Antonov, *World Ocean Atlas 1994*, vol. 5, *Interannual Variability of Upper Ocean Thermal Structure, NOAA Atlas NESDIS*, vol. 5, 176 pp., Natl. Oceanic and Atmos. Admin., Silver Spring, Md., 1994b.

Losier, M. S., W. B. Owens, and R. G. Curry, The climatology of the North Atlnatic, *Prog. Oceanogr.*, *36*, 1–44, 1995.

Marotzke, J., and C. Wunsch, Finding a steady state of general circu-

lation model through data assimilation: Application to the North Atlantic ocean, *J. Geophys. Res.*, *98*, 20,149–20,167, 1993.

Martel, F., and C. Wunsch, The North Atlantic circulation in the early 1980's: An estimate from inversion of a finite difference model, *J. Phys. Oceanogr.*, *23*, 898–924, 1993.

Mercier, H., M. Ollitrault, and P. Y. Le Traon, An inverse model of the North Atlantic general circulation using Lagrangian float data, *J. Phys. Oceanogr.*, *23*, 689–715, 1993.

Nechaev, D. A., M. I. Yaremchuk, and K. Thompson, On determination of the large-scale circulation in an open ocean region by the variational method, *Oceanology*, *35*, 311–319, 1995.

Needler, G. T., A model for the thermohaline circulation in an ocean of finite depth, *J. Mar. Res.*, *25*, 329–342, 1967.

Provost, C., and R. Salmon, A variational method for inverting hydrographic data, *J. Mar. Res.*, *44*, 1–34, 1986.

Rossby, T., The North Atlantic Current and surrounding waters: At the crossroads, *Rev. Geophys.*, *34*, 463–481, 1996.

Schlitzer, R., Determining the mean large-scale circulation of the Atlantic with the adjoint method, *J. Phys. Oceanogr.*, *23*, 1935–1974, 1993.

Schmitt, R. V., P. S. Bogden, and C. E. Dorman, Evaporation minus precipitation and density fluxes for the North Atlantic, *J. Phys. Oceanogr.*, *19*, 1208–1221, 1989.

Schmitz, W. J., and M. S. McCartney, On the North Atlantic circulation, *Rev. Geophys.*, *31*, 29–49, 1993.

Stommel, H., and F. Schott, The β-spiral and the determination of the absolute velocity field from hydrographic data, *Deep Sea Res.*, *24*, 325–329, 1977.

Sy, A., Investigation of large-scale circulation patterns in the central North Atlantic: The North Atlantic Current, the Azores current and the Mediterranean Water plume in the area of the Mid-Atlantic Ridge, *Deep Sea Res., Part A*, *35*, 383–413, 1988.

Sy, A., V. Schauer, and J. Meincke, The North Atlantic Current and its associated hydrographic structure above and eastwards of Mid Atlantic Ridge, *Deep Sea Res., Part A*, *39*, 825–853, 1992.

Tai, C.-K., and W. B. White, Eddy variability in the Kuroshio Extension as revealed by Geosat altimetry: Energy propagation away from the jet—Reynolds stress and seasonal cycle, *J. Phys. Oceanogr.*, *20*, 1761–1777, 1990.

Tapley, B. D., D. P. Chambers, C. K. Shum, R. J. Eans, and J. C. Ries, Accuracy assessment of the large-scale dynamic ocean topography from TOPEX/Poseidon altimetry, *J. Geophys. Res.*, *99*, 24,605–24,617, 1994.

Thacker, W. C., Fitting models to inadequate data by enforcing spatial and temporal smoothness, *J. Geophys. Res.*, *93*, 10,556–10,566, 1988.

Thacker, W. C., On the role of Hessian matrix in fitting models to data, *J. Geophys. Res.*, *94*, 6177–6196, 1989.

Welander, P., An advective model of the ocean thermocline, *Tellus*, *11*, 309–318, 1959.

Wunsch, C., Dynamically consistent hydrography and absolute velocity in the eastern North Atlantic Ocean, *J. Geophys. Res.*, *99*, 14,071–14,090, 1994.

Yaremchuk, M. I., D. A. Nechaev, J. Schröter, and E. Fahrbach, A dynamically consistent analysis of circulation and transports in the southwestern Weddell Sea, *Annal. Geophys.*, *16*, 1024–1038, 1998.

D. A. Nechaev, Department of Marine Science, University of Southern Mississippi, Stennis Space Center, MS 39529.

K. R. Thompson, Department of Oceanography, Dalhousie University, Halifax, N. S. B3H 4J1, Canada.

M. I. Yaremchuk, International Pacific Research Center, University of Hawaii, 2525 Correa Road, Honolulu, HI 96822. (maxy@soest.hawaii.edu)